

## Reactive magnetron synthesis and study of the structure and optical properties of thin-film tungsten oxide doped with molybdenum

© I.F. Malikov,<sup>1,2</sup> N.M. Lyadov,<sup>1</sup> M.Kh. Salakhov,<sup>2</sup> L.R. Tagirov<sup>1</sup>

<sup>1</sup> Zavoisky Physical-Technical Institute, FRC KazSC of RAS,  
420029 Kazan, Russia

<sup>2</sup> Institute of Physics, Kazan Federal University,  
420008 Kazan, Russia  
e-mail: ltagirov@mail.ru

Received December 14, 2022

Revised October 21, 2023

Accepted October 22, 2023

Cationic doping of tungsten oxide with molybdenum was applied to obtain an electrochromic cathode material, the spectral transmission of which can be controlled by the doping level. A series of samples was synthesized by reactive magnetron co-sputtering of metallic tungsten and molybdenum in a mixture of argon and oxygen gases. Morphology, structure, elemental and valence composition of constituent elements of the films were characterized by scanning electron microscopy, X-ray diffraction, energy-dispersive X-ray spectroscopy, and X-ray photoelectron spectroscopy. Optical properties were measured using transmission spectrophotometry and spectroscopic ellipsometry. With an increase in the doping level, the resulting films acquire a gray color and become low-transparent. The ellipsometric studies have shown that enhancement of the absorption occurs both in the short-wavelength and long-wavelength parts of the visible light and adjacent parts of the spectrum. This leads to a mutual compensation of colorings, resulting in an almost achromatic change in the optical transmission and thus improving the consumer qualities of the electrochemical material and devices based on tungsten oxide.

**Keywords:** electrochromism, tungsten trioxide, doping with molybdenum, optical transmission, spectroscopic ellipsometry.

DOI: 10.61011/JTF.2024.01.56904.274-23

### Introduction

Electrochromism is a phenomenon when the transparency as well as the color of a material change when an electric voltage is applied to it as part of an electrochemical cell (see [1–7] and references therein). This phenomenon can be potentially used in architectural glazing, interior design, and the automotive industry, but it has not yet found mass application, since it is necessary to ensure the long-term stability of many parameters of electrochromic products in harsh operating conditions: high and low temperatures with large gradients, prolonged intense exposure to direct sunlight, as well as glass tinting color pattern perceived by the customers (see [8–11] and references therein). Therefore, electrochromic glass is still used in the form of interior rear-view mirrors of cars of some brands, electronic window blinds of some aircraft models and in other non-mass products. Efforts are taken to improve the performance of electrochromic devices, the rate of coloration/bleaching durability and the number of switches between colored and bleached states.

Tungsten trioxide  $\text{WO}_3$  ( $\text{WO}_{3-x}$ ) [12] is one of the most studied cathode electrochromic materials, the optical density of which changes in case of intercalation by protons ( $\text{H}^+$ ), ions of alkaline elements (Li, K, Na) and alkaline earth

elements (Al) that are contained in the electrolyte of the electrochromic cell ([2–6,10] and references therein).  $\text{WO}_{3-x}$  is an inorganic material that is highly resistant to prolonged exposure to sunlight and high temperatures, however, the time of transition from the bleached state to the colored state and back strongly depends on the method of preparation of films based on tungsten oxide, their composition, and can reach several minutes. Moreover, the darkened/colored state is characterized by an intense blue color, which is not always acceptable for the particular purpose of electrochromic glass technology.

The doping of tungsten oxide with elements of other metals may be one of the methods to control the color tone of staining and its dynamic range. It also exhibits an electrochromic effect with coloring in warm colors (the long-wavelength part of the visible light spectrum). Such doping may result in a redistribution of the spectral light absorption density of the main ion and a shift in the visual assessment of the color towards neutral (achromatic). Finally, doping can also change the micro- and nanostructure of the base tungsten oxide material and thereby affect the process of intercalation/deintercalation of ions from the electrolyte [10]. The base material  $\text{WO}_{3-x}$  can be doped with both anions and cations because of its composite nature. We synthesized tungsten oxynitride and analyzed the anionic doping of  $\text{WO}_{3-x}$  with nitrogen in previous

**Table 1.** Sputtering conditions and sample properties

Sample №	Flow Ar, sccm	Flow O <sub>2</sub> , sccm	Chamber Pressure, Pa	Thickness Film, nm	Visible Transmission Light, %	Color film
231	183	17	3.07 (23 mTorr)	433	29.3	Dark grey
221	183	17	3.20 (24 mTorr)	370	47.6	Grey
216	183	17	3.33 (25 mTorr)	331	59.9	Light grey
215	183	17	3.47 (26 mTorr)	318	68.6	Smoky grey
214	183	17	3.87 (29 mTorr)	263	75.8	Transparent bluish

studies [13]. We applied molybdenum cationic doping in this work and studied the micro- and nanostructure of the resulting material and the change of its optical properties with a variation of the doping level.

## 1. Preparation of samples, their morphology, structure and elemental analysis

### 1.1. Preparation of samples

Thin films of nonstoichiometric tungsten oxide doped with molybdenum ( $W_yMo_xO_{3-x} \equiv WMO$ ) were grown by reactive magnetron co-sputtering in an atmosphere of a high purity reactive plasma gas comprising argon (plasma gas, flow rate 183 cm<sup>3</sup>/min (Table. 1)) and oxygen (reactive gas, flow rate 17 cm<sup>3</sup>/min (Table. 1)). The pressure of the gas mixture in the vacuum chamber varied from sample to sample in the range of 3–4 Pa (Table. 1) and was automatically maintained throughout each deposition cycle. Sputtering was performed from high purity tungsten and molybdenum metal targets (99.9% Girmet), the constant power at the level of 300 W for W and 150 W for Mo was supplied to the magnetrons. A microscopy slide polished on both sides with a size of 76 × 26 mm and a thickness of 1 mm was used as a substrate for sputtering. It was pre-cleaned in an aqueous solution of sodium alkylbenzenesulfonate, EDTA tetranatrium and sodium pyrophosphate using an ultrasonic bath. The following samples were synthesized (Table. 1): sample № 231 was obtained at a pressure of 3.07 Pa (23 mTorr); № 221 was obtained at a pressure of 3.20 Pa (24 mTorr); № 216 was obtained at a pressure of 3.33 Pa (25 mTorr); № 215 was obtained at a pressure of 3.47 Pa (26 mTorr); № 214 was obtained at a pressure of 3.87 Pa (29 mTorr).

The prepared films were cut into several parts for further studies after evacuation from the vacuum chamber, in particular, one fragment of each initial sample was annealed in a muffle furnace in an air atmosphere using the following sequence: 2 h of heating from room temperature to 673 K (400°C), then annealing during 10 h at 673 K and cooling during 4 h to room temperature. Further, annealed samples are marked with the suffix „t“,

for example № 231t, and samples subjected to ion etching are designated with the suffix „e“, for example № 231e.

### 1.2. Scanning electron microscopy and X-ray diffraction analysis

The morphology of the obtained films was studied using a scanning electron microscope (SEM) by Carl Zeiss Merlin and showed a mesoporous surface structure of synthesized samples with dimensional features of a submicron scale of about 100–200 nm in sample No 131 and less than 50 nm in sample № 214 (Fig. 1, *a* and *d*, respectively). Annealing of the samples resulted in the crystallization of the film material, however, without pronounced texturing (Fig. 1, *b* and *e*). The morphology of the surface is similar to the morphology of the surface obtained after annealing of the thin-film heterostructure WO<sub>3</sub>/MoO<sub>3</sub> at 473 K [14].

Rigaku SmartLab diffractometer with Cu  $K_{\alpha 1}$ -radiation ( $\lambda = 1.54059 \text{ \AA}$ ) was used for X-ray diffraction analysis (XRD) in Bragg–Brentano geometry; beam angle of incidence was 0.3°, angle step was 0.02° and scanning rate was 2 s per point; range of angles  $2\theta$  from 10 to 60°. The diffractogram was processed using the PDXL-2 firmware and ICDD PDF-2 database of crystalline compounds. The analysis showed that the glass substrate, being an amorphous material in general, exhibits the presence of a short-range order in the arrangement of atoms (a wide asymmetric peak in the area of angles  $2\theta \sim 15\text{--}38^\circ$ ). The diffractogram of the WMO film on the substrate after annealing also exhibits a broad peak of the amorphous material in a narrower range of angles  $2\theta \sim 20\text{--}33^\circ$ . A wide short-range peak in the glass substrate is suppressed due to the absorption of X-ray radiation in the film (Fig. 1). Peaks were observed on the sample diffractogram after annealing, suggesting the crystallization of the initially amorphous film material for a thicker film of sample No 231 and the reaction product of the initial film material with a glass substrate (sample No 214t).

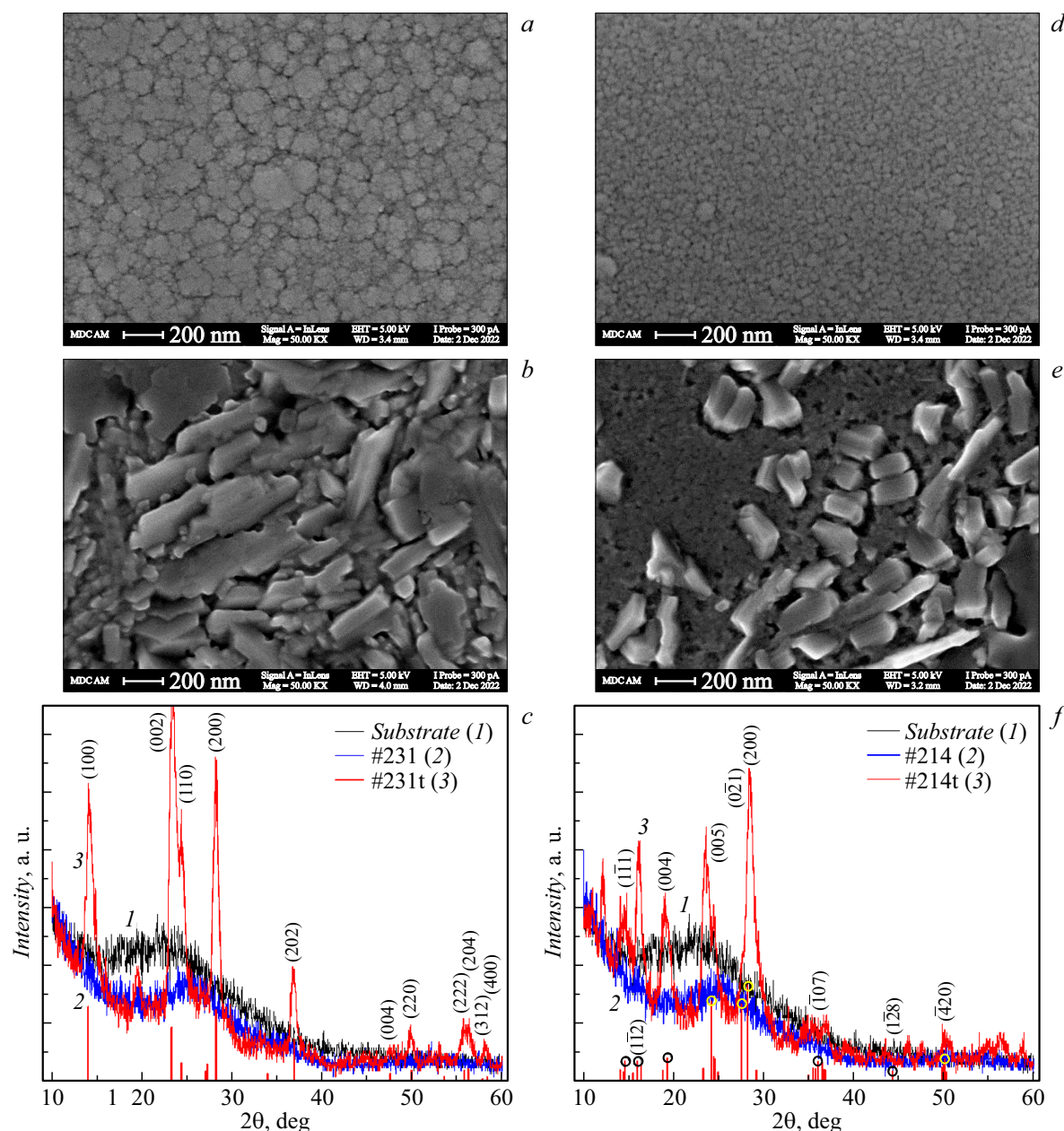


**Figure 1.** Images of samples № 231 (*a, b*) and № 214 (*d, e*) acquired using scanning electron microscopy. X-ray patterns of samples: *c* — № 231, *f* — № 214. The following signals are designated by numbers: 1 — substrate, 2 — unannealed sample, 3 — annealed sample; *c* — the most intensive reflexes of the powder hexagonal ( $P63/mcm$ )  $WO_3$ ; *f* — the most intensive reflexes of the dominant phase of the powder  $Na_5W_{14}O_{44}$  are marked.

### 1.3. Elemental analysis

The elemental analysis was performed using the energy dispersive X-ray spectroscopy system (EDX) Oxford Inca Energy 350 with Carl Zeiss EVO50 XVP scanning electron microscope. It showed the presence of elements of the WMO film in atomic percentage, listed in Table 2. It shows that the degree of molybdenum doping (the fourth and last columns of Table 2) increases monotonously within the measurement error from 2.6 to 5.4 at.% (after deposition) and from 2.5 to 4.5 at.% (after annealing) with a decrease

in the pressure of the gas mixture in the vacuum chamber during film deposition.

## 2. Valence composition and optical measurements

### 2.1. X-ray photoelectron spectroscopy

The X-ray photoelectron spectroscopy (XPS) was used for elemental composition and valence analysis. The XPS is designed for surface and near-surface studies unlike

**Table 2.** Elemental composition of samples according to EDRS data (the averaged data of three surface areas for each of samples are given)

Sample №	After deposition, at.%			Annealed, at.%		
	W	O	Mo	W	O	Mo
231	18.2	76.4	5.4	18.4	77.1	4.5
221	16.4	79.9	3.8	17.6	78.7	3.7
216	17.6	78.8	3.6	17.5	79.2	3.3
215	16.9	80.3	2.8	17.6	79.2	3.2
214	17.7	79.8	2.6	14.9	82.6	2.5

the EDX method, since the scanning depth is several nanometers. The advantage of the XPS method over EDX is its ability to determine the valence composition of the studied material. Obviously, the substrate does not contribute to the signal from the film with its thickness of 250–450 nm.

The XPS system operates at a base pressure of  $3 \cdot 10^{-8}$  Pa, it has a Mg- $K_{\alpha}$  X-ray source operating with a voltage of 12.5 kV and power of 250 W, and it is provided with hemispherical photovoltaic energy analyzer Phoibos 150 (all provided by SPECS). The survey XPS spectra were recorded in the range 0–1000 eV with an energy increment of 1 eV and a transmittance energy of 80 eV. High-resolution spectra were recorded in the energy ranges of interest by averaging over 100 scans for three elements with energy increments of 0.1 eV and transmittance energy of 20 eV [15]. The system is also provided with an integrated surface etching option with a wide, inclined beam of argon ions of varying energy for depth profiling [16].

Fig. 2 shows the survey XPS spectrum of sample No 231 and the high-resolution spectra separately for W4f, Mo3d and O1s (see caption to the figure) together with their decomposition into valence components in the initial sample No 231 and the same sample after 1620 s of argon etching No 231e. We do not provide element-by-element spectra for other samples, including annealed samples, because they are practically the same in terms of tungsten and molybdenum and show a doublet for the degree of oxidation 6+. Only the ratio of stoichiometric and non-stoichiometric oxygen significantly differs in the series of non-annealed and annealed samples.

The XPS tungsten spectrum contains one doublet of valence 6+ (35.8 and 37.9 eV) of sample No 231, and 3 doublets of sample No 231e corresponding to the degree of oxidation 6+, 5+ and 4+ with binding energies of 35.8 and 37.9 eV, 33.5 and 35.6 eV, 31.9 and 34 eV, respectively [17–19].

The kinetics of molybdenum ion etching is significantly faster compared to the tungsten etching

(Fig. 2, c and f). Only the degree of oxidation Mo<sup>6+</sup> (232.4 and 235.7 eV) [20,21] is present in the initial sample No 231, only Mo<sup>4+</sup> (229.3 and 232.6 eV) remains after 1620 s of etching [22].

Fig. 3 shows the XPS spectra of intermediate etching stages only for W and Mo which demonstrate that the intensity of the molybdenum signal in the valence 6+ rapidly decreases with the synchronous emergence and increase of the proportion of the degree of oxidation Mo<sup>4+</sup> and the complete absence of a signal from the valence 5+ within the sensitivity of the spectrometer (nominally 0.1%) unlike tungsten, which exhibits a gradual decrease of the proportion of valence 6+ with the sequential emergence and increase of the signal from the degrees of oxidation 5+ and 4+.

The oxygen XPS line is generally asymmetric (Fig. 2, d and g), it can be decomposed into oxygen in a stoichiometric environment in a crystal WO<sub>3</sub> (maximum binding energy — 530.8 eV) and in a non-stoichiometric environment (maximum binding energy — 532.3 eV) [14,17,22]. The signal of oxygen chemically bound to molybdenum cannot be identified because of the low content of the Mo and the superposition of peaks from the W–O and Mo–O bonds.

## 2.2. Optical properties

Fig. 4 shows images of the samples after deposition (Fig. 4, a–e). Visually, the sample No 231 has a dark gray color; sample No 221 has a gray color; sample No 216 is light gray; sample No 215 is smoky gray; sample No 214 is transparent bluish. The integral transmittance of light through a WMO film was studied using UV/VIS/NIR Perkin Elmer Lambda 1050 spectrophotometer in the visible wavelength range of 0.38–0.78  $\mu\text{m}$  in transmission geometry and is presented in Table 1, in the next-to-last column.

The optical absorption and refraction were studied in more detail using spectroscopic ellipsometry (Woollam VASE) in 0.25–2.5  $\mu\text{m}$  wavelength range in the reflection geometry. The measurements were performed at the angles of incidence of the optical axis of the collimated radiation 55 and 75°. The transmittance coefficient was also measured in the same wavelength range in the transmission geometry.

Fig. 4, f and g shows the dependence of refraction indexes  $n$  and extinction  $k$  on the wavelength and Fig. 4, h shows the spectroscopic transparency of the samples. It is apparent, the relative absorption at short wavelengths and, especially, in the region of long waves with a maximum in the orange region and a tightened tail in the near-infrared range significantly increases in the range of the studied wavelengths of 0.25–2.5  $\mu\text{m}$  with an increase of the molybdenum content (Fig. 4, g). It is also apparent, based on the dependence of the transmittance coefficient on the wavelength (Fig. 4, h) that the transmittance is on average close to constant and is strongly attenuated in

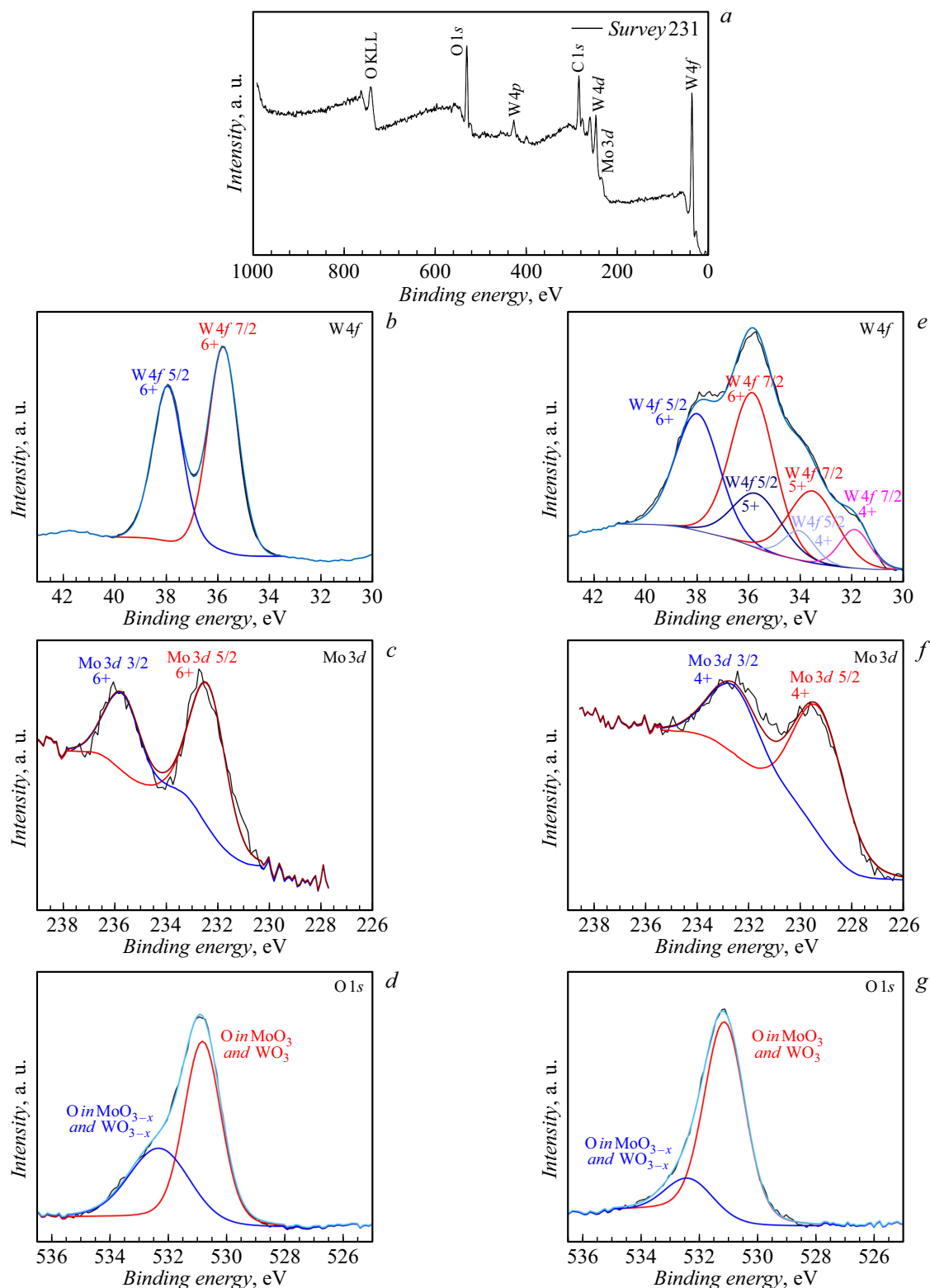


**Figure 2.** The results of the XPS measurements. *a* — survey spectrum showing the contribution of all elements of the WMO film; *b-d* — sample No 231; *e-g* — same sample after 1620s surface etching with argon (No 231e). The decompositions into contributions from ions with different valence are shown.

sample No 231 with the maximum molybdenum content in the visible wavelength range, which determines its dark gray, almost achromatic color (transmittance coefficient

oscillations are caused by interference in a thin film of the studied electrochromic material). This property persists in sample No 215 with a monotonous increase of overall

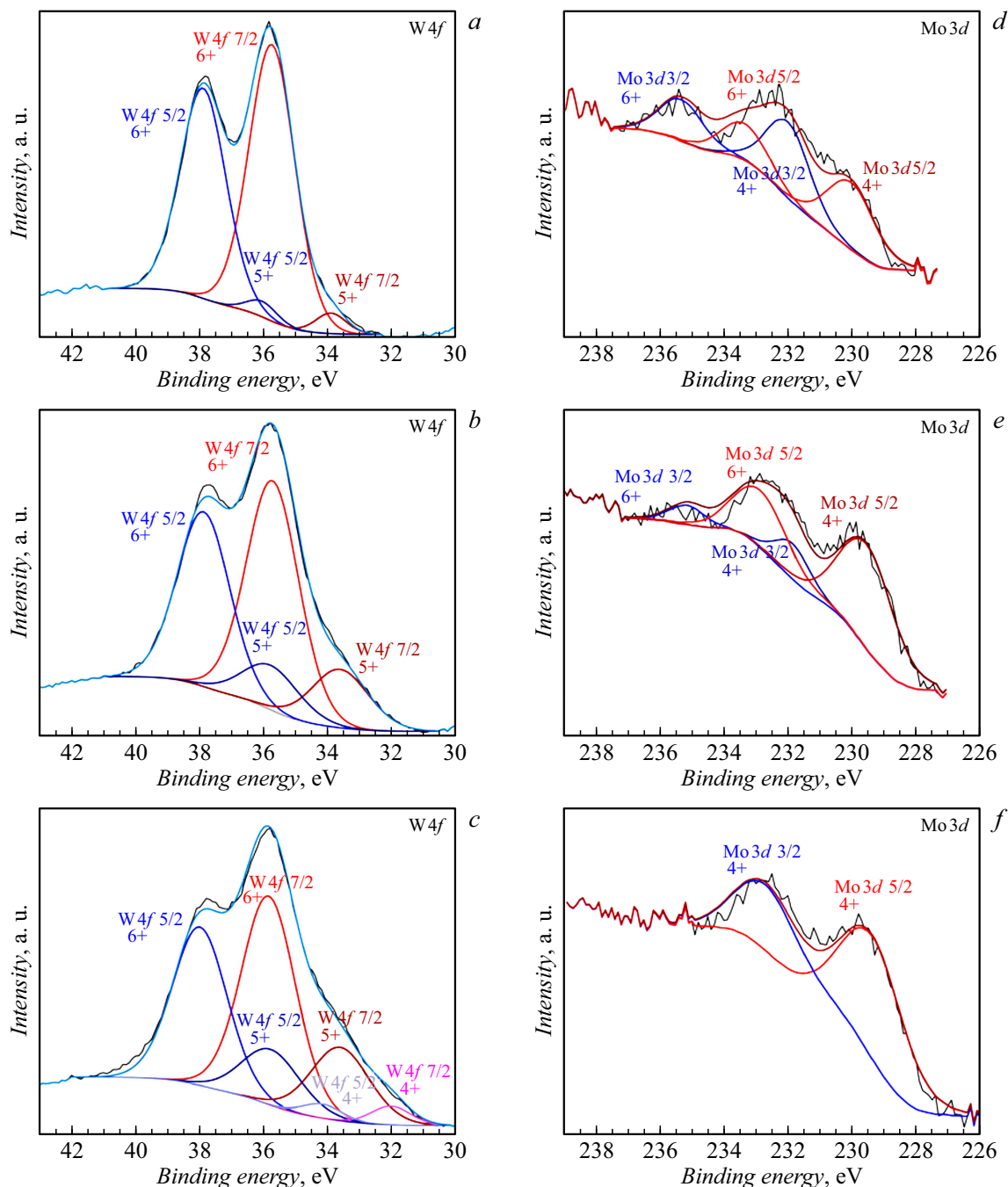


**Figure 3.** Evolution of XPS spectra during the argon ion etching process. Left column — evolution of the tungsten spectrum during the etching process: *a* — 60; *b* — 360; *c* — 720 s. Right column — evolution of the molybdenum spectrum during the etching process: *d* — 60; *e* — 360; *f* — 720 s.

transparency. The proportion of transmission of short-wave radiation increases in sample No 214 vs. sample No 215, which results in the blue hue.

### 3. Results and discussion

Visually, the effect of coloring in neutral tones was observed with an increase of the level of doping of tungsten

oxide with molybdenum starting from transparent bluish to dark gray through shades of gray with intermediate intensity. SEM images show a systematic reduction of the grain size of the film surface with a decrease of the degree of molybdenum doping with a slight increase of the pressure in the vacuum chamber during film deposition. The X-ray diffraction measurements (Fig. 1, *c* and *f*) demonstrated that predominantly amorphous films of doped tungsten oxide were grown (possibly small and severely defective

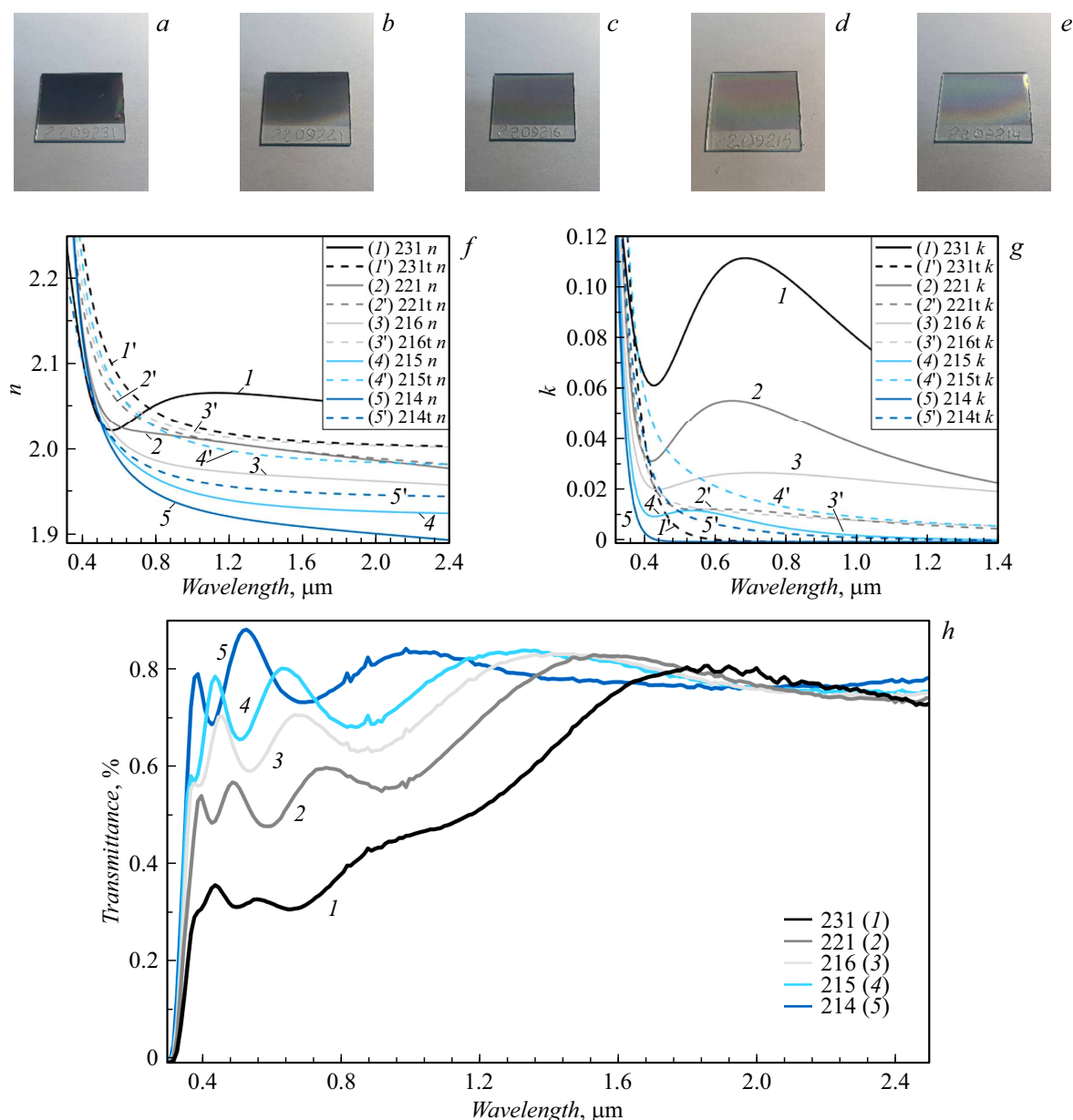


**Figure 4.** Images of samples No 231 (a), No 221 (b), No 216 (c), No 215 (d), No 214 (e). Results of spectroscopic ellipsometry: *f* — dependence of the refractive index  $n$  on wavelength; *g* — dependence of the attenuation coefficient (extinction)  $k$  on wavelength; *h* — dependence of the transmission coefficient on the wavelength.

nanocrystallites against the background of an amorphous material), blue lines with wide peaks of the near order with maxima near  $2\theta \approx 25^\circ$  and  $\approx 36^\circ$ . The film annealing resulted in the partial crystallization of the initially amorphous films [10,14,23,24], and the crystalline phase of the thickest film of the sample No 231t best corresponds to the structure of the powder hexagonal ( $P63/mcm$ )  $\text{WO}_3$  (Fig. 1, c). The thinnest of five films (sample No 214t) partially reacted with the substrate glass during annealing, so that the dominant crystalline phase best corresponds to the structure of the powder  $\text{Na}_5\text{W}_{14}\text{O}_{44}$  (Fig. 1, f).

A significant change of the morphology of molybdenum-doped tungsten oxide films was also found during

thermal annealing. It affects the rate of intercalation/deintercalation by electrolyte ions. Therefore, the rate of coloration/bleaching can be optimized by selecting electrochromic material heat treatment conditions.

XPS measurements showed that a significant difference in the oxidation of W and Mo ions is possible in case of doping of tungsten oxide with molybdenum (see below). The experiments with the argon etching of the film surface for deep profiling showed that tungsten is present in three degrees of oxidation throughout the etching depth, 6+, 5+ and 4+ even in case of the etching time of 1620 s (Fig. 2, e), whereas only traces of valence  $\text{Mo}^{6+}$  remain already for the etching time of 360 s and the signal  $\text{Mo}^{6+}$  disappears

with further etching being completely replaced by the signal of  $\text{Mo}^{4+}$  (Fig. 3,f). The degree of oxidation  $\text{Mo}^{5+}$  is not observed at all within the spectrometer sensitivity limits, unlike thin-film heterostructural Mo-oxide/W-oxide [20] and molybdenum oxide films  $\text{MoO}_3$  [21].

The results of depth profiling described above should not be taken literally as the distribution of W and Mo valence states in depth from the surface of the film because of the selectivity of etching due to the large difference of masses of the oxygen ion and ions of refractory metals. It results in a partial reduction of metal ions with the increase of the etching time. However, it could be possible to expect a higher selectivity and faster reduction of tungsten ions compared with molybdenum based on the comparison of the difference in the masses of oxygen ions (16, Da), Mo (96, Da) and W (184, Da), whereas the opposite happens (Fig. 3). The contributions of changes of the degree of oxidation by depth and selective etching cannot be distinguished, since there is no control (reference) sample with a homogeneous composition in depth. Annealed samples have radically different morphology, therefore they cannot be used as control samples.

The study of optical properties by transmission spectrophotometry and spectroscopic ellipsometry showed that cationic doping of tungsten oxide with molybdenum increases the relative absorption in the short-wavelength (from blue to UV) range with simultaneous enhancement of absorption in the long-wavelength part of the visible and near-infrared range. The increased absorption at the edges of the visible range is largely compensated in terms of coloration, resulting in an almost achromatic change of the optical transmittance, opening up areas for improvement of the consumer performance of electrochemical materials and devices based on molybdenum-doped tungsten oxide.

## Funding

The study of I.F. Malikov, N.M. Lyadov and L.R. Tagirov were funded by the Russian Science Foundation, project no. 22-22-00980.

## Acknowledgments

The authors sincerely thank V. Meshcheryakov, V. Chugunov, M. Ermakov, R. Batulin, I. Vakhitov, A. Gumarov, L. Nurtdinova, A. Rogov, I. Tverdov and R. Yusupov for valuable assistance in preparation of samples and measurements. X-ray diffraction studies were performed using the equipment of the CCU „Nanomaterials and Nanotechnology“ of Kazan National Research Technological University.

## Conflict of interest

The authors declare that they have no conflict of interest.

## References

- [1] S.K. Deb. *Appl. Opt.*, **8**, 192 (1969). DOI: 10.1364/AO.8.S1.000192
- [2] C.G. Granqvist. *Handbook of Inorganic Electrochromic Materials* (Elsevier, Amsterdam, 2002)
- [3] P.M. Monk, R.J. Mortimer, D.R. Rosseinsky. *Electrochromism and Electrochromic Devices* (Cambridge University Press, Cambridge, 2007), v. 421. [www.cambridge.org/9780521822695](http://www.cambridge.org/9780521822695)
- [4] G.A. Niklasson, C.G. Granqvist. *J. Mater. Chem.*, **17**, 127 (2007). DOI: 10.1039/B612174H
- [5] T. He, J. Yao. *J. Mater. Chem.*, **17**, 4547 (2007). DOI: 10.1039/B709380B
- [6] D.T. Gillaspie, R.C. Tenent, A.C. Dillon. *J. Mater. Chem.*, **20**, 9585 (2010). DOI: 10.1039/c0jm00604a
- [7] A.L. Belousov, T.N. Patrusheva. *J. Siberian Federal University. Eng. Technol.*, **7**, 154 (2014).
- [8] C.G. Granqvist. *Mater. Today: Proceed.*, **3**, S2 (2016). DOI: 10.1016/j.matpr.2016.01.002
- [9] V.A. Maiorov. *Opt. Spectrosc.*, **126**, 412 (2019). DOI: 10.1134/S0030400X19040143
- [10] Sh. Zeb, G. Sun, Y. Nie, H. Xu, Y. Cui, X. Jiang. *Mater. Adv.*, **2**, 6839 (2021). DOI: 10.1039/D1MA00418B
- [11] C.G. Granqvist. *Eco-Efficient Materials for Reducing Cooling Needs in Buildings and Construction. Design, Properties and Applications*, ed. by F. Pacheco-Torgal, L. Czarnecki, A.L. Pisello, L.F. Cabeza (Elsevier, Amsterdam, 2021)
- [12] Electronic media. Available at: [http://database.iem.ac.ru/minicryst/s\\_carta.php?OXIDE\\_W+3412](http://database.iem.ac.ru/minicryst/s_carta.php?OXIDE_W+3412)
- [13] I.F. Malikov, N.M. Lyadov, M.Kh. Salakhov, L.R. Tagirov. *Crystals (MDPI)*, **14**, 109 (2024). DOI: 10.3390/cryst14020109
- [14] R.R. Kharade, S.S. Mali, S.S. Mohite, V.V. Kondalkar, P.S. Patil, P.N. Bhosale. *Electroanalysis*, **26**, 2388 (2014). DOI: 10.1002/elan.201400239
- [15] A. Esmacili, I.V. Yanilkin, A.I. Gumarov, I.R. Vakhitov, B.F. Gabbasov, A.G. Kiiamov, A.M. Rogov, Yu.N. Osin, A.E. Denisov, R.V. Yusupov, L.R. Tagirov. *Thin Solid Films*, **669**, 338 (2019). DOI: 10.1016/j.tsf.2018.11.015
- [16] A.I. Gumarov, I.V. Yanilkin, R.V. Yusupov, A.G. Kiiamov, L.R. Tagirov, R.I. Khaibullin. *Mater. Lett.*, **305**, 130783 (2021). DOI: 10.1016/j.matlet.2021.130783
- [17] O. Bouvard, A. Krammer, A. Schüller. *Surf. Interface Anal.*, **48**, 660 (2016). DOI: 10.1002/sia.5927
- [18] B. Yang, P. Miao. *J. Cui. J. Mater. Sci.: Mater. Electron.*, **31**, 11071 (2020). DOI: 10.1007/s10854-020-03656-5
- [19] H.T.T. Nguyen, Th.H. Truong, T.D. Nguyen, V.Th. Dang, T.V. Vu, S.T. Nguyen, X.Ph. Cu, Th.T.O. Nguyen. *J. Mater. Sci.: Mater. Electron.*, **31**, 12783 (2020). DOI: 10.1007/s10854-020-03830-9
- [20] S. Xie, D. Chen, Ch. Gu, T. Jiang, Sh. Zeng, Y.Y. Wang, Zh. Ni, X. Shen, J. Zhou. *ACS Appl. Mater. Interfaces*, **13**, 33345 (2021). DOI: 10.1021/acsami.1c03848
- [21] Q. Han, R. Wang, H. Zhu, M. Wan, Ya. Mai. *Mater. Sci. Semicond. Process.*, **126**, 105686 (2021). DOI: 10.1016/j.mssp.2021.105686
- [22] J. Liu, S. Tang, Y. Lu, G. Cai, Sh. Liang, W. Wang, X. Chen. *Energy Environ. Sci.*, **6**, 2691 (2013). DOI: 10.1039/c3ee41006d
- [23] M. Righettoni, S.E. Pratsinis. *Mater. Res. Bull.*, **59**, 199 (2014). <http://dx.doi.org/10.1016/j.materresbull.2014.07.018>
- [24] J. Ram, R.G. Singh, R. Gupta, V. Kumar, F. Singh, R. Kumar. *J. Electron. Mater.*, **48**, 1174 (2019). DOI: 10.1007/s11664-018-06846-4

Translated by A.Akhtyamov